

## Thermodynamic Structure of the Solar Corona: Tomographic Reconstructions and MHD Modeling

Diego G. Lloveras<sup>1</sup>  · Alberto  
M. Vásquez<sup>1,2</sup>  · Federico A. Nuevo<sup>1,3</sup>  ·  
Cecilia Mac Cormack<sup>1,2</sup>  ·  
Nishtha Sachdeva<sup>4</sup>  · Ward Manchester  
IV<sup>4</sup>  · Bartholomeus Van der Holst<sup>4</sup>  ·  
Richard A. Frazin<sup>4</sup> 

© Springer ....

**Abstract** Observational techniques play an essential role in advancing our understanding of the physics of the solar corona. They provide validation data

- 
- ✉ D.G. Lloveras  
dlloveras@iafe.uba.ar
  - ✉ A.M. Vásquez  
albert@iafe.uba.ar
  - ✉ F.A. Nuevo  
federico@iafe.uba.ar
  - ✉ C. Mac Cormack  
cmaccormack@iafe.uba.ar
  - ✉ N. Sachdeva  
nishthas@umich.edu
  - ✉ W. Manchester IV  
chipm@umich.edu
  - ✉ B. Van der Holst  
bartvand@umich.edu
  - ✉ R.A. Frazin  
rfrazin@umich.edu

<sup>1</sup> Instituto de Astronomía y Física del Espacio (IAFE), CONICET-UBA, CC 67 - Suc 28, (C1428ZAA) Ciudad Autónoma de Buenos Aires, Argentina

<sup>2</sup> Universidad Nacional de Tres de Febrero (UNTREF). Departamento de Ciencia y Tecnología, Sáenz Peña, Argentina.

<sup>3</sup> Ciclo Básico Común (CBC), Universidad de Buenos Aires (UBA), Buenos Aires, Argentina

<sup>4</sup> Department of Climate and Space Sciences and Engineering (CLaSP), University of Michigan, 2455 Hayward Street, Ann Arbor, MI 48109-2143, USA

for three-dimensional (3D) magnetohydrodynamic (MHD) models of the solar atmosphere, key to improve their space weather forecasting capabilities. Solar rotational tomography (SRT) is currently the sole observational technique that provides an empirical 3D description of some of the fundamental plasma parameters of the solar corona at a global scale. Based on EUV data of space borne instruments, SRT allows constructing 3D maps of the coronal electron density and temperature at heliocentric heights below 1.25 R<sub>sun</sub>. We carry out a study of the corona combining tomographic reconstructions with MHD simulations using the latest version of the Alfvén Wave Solar Model (AWSoM) of the Space Weather Modeling Framework (SWMF). Target rotations were selected from the solar minimum between solar cycles (SC) 23 and 24 and the current declining phase of solar cycle 24. Tomographic reconstructions and results of the model are analysed in distinct coronal magnetic structures. We study magnetically closed structures associated with the equatorial streamer belt, as well as magnetically open regions enclosing it. We report on the tomographic results in the different structures, their implications for the physics of the solar corona, and the current capability of the AWSoM model to reproduce the tomographic reconstructions in different regions.

**Keywords:** Solar Cycle, Observations; Corona,E; Corona, Structures

## 1. Introduction

Being the place where the solar atmosphere is heated and the solar wind accelerated, and where impulsive events such as solar flares and coronal mass ejections are energized, observation and modeling of the solar corona are tasks of great relevance to improve our understanding of the Sun-Earth environment. To advance our knowledge of the physics of the solar corona, as well as to improve its three-dimensional (3D) models, information derived from observational data plays a key role. Solar rotational tomography is currently the sole observational technique able to provide a quantitative empirical description of the 3D distribution of some fundamental plasma parameters of the solar corona at a global scale.

NOTE: Here we will put in a couple of paragraphs summarizing what SRT and DENT are, including references and defining the accronyms in the process. We should refer to minima in particular. We should mention the instruments and missions we use as data for DENT, and define their accronyms too. Also, a couple of paragraphs on the AWSoM model and the SWMF, including references and defining the accronyms in the process.

Based on time-series of EUV images, differential emission measure tomography (DEMT) allows reconstruction of the 3D distribution of the differential emission measure (DEM) of the solar corona. The technique was first developed by Frazin, Vásquez, and Kamalabadi (2009), and first applied to the observational study of coronal structures by Vásquez, Frazin, and Kamalabadi (2009). In DEMT, the low corona in the height range  $1.0 - 1.25 R_{\odot}$  is discretized in a spherical computational grid. The size of the tomographic cell (or voxel) is

---

typically set to  $0.01 R_{\odot}$  in the radial direction and  $2^{\circ}$  in both the latitudinal and longitudinal directions. The cadence of the data time-series is set to 6 hr. The main product of the technique is the local DEM (LDEM), a measure of the temperature distribution of the plasma contained in each voxel of the tomographic grid. A recent review by Vásquez (2016) summarizes the DMT works up until then. More recently Lloveras *et al.* (2017) applied DMT to study the last two solar minima, and Mac Cormack *et al.* (2017) developed a new DMT product concerning the energetics of the inner solar corona.

## 2. Methodology

### 2.1. DMT Reconstructions

We carried out the 3D DMT reconstruction and MHD modeling of two target Carrington rotations (CR). We selected CR-2082 (2009, 05 April through 03 May), a deep minimum rotation between solar cycles (SC) 23 and 24, and CR-2208 (2018, 02 September through 29 September), a rotation during the early declining phase of SC 24. To study CR-2082 and CR-2208 data taken by the STEREO/EUVI-B/STEREO and SDO/AIA instruments was used, respectively. The EUVI and AIA data were prepared using the latest processing tools and calibration corrections provided by their teams through the SolarSoft package. For this work, we introduced two improvements in the implementation of the DMT technique, as described next.

While in all previous DMT studies full-disk data was used to perform tomography, in this work we opted to only use off-limb data. In this way, the smallest scale and brighter coronal features seen on disk (most typically in the  $171\text{\AA}$  band) are not included. This has two implications. Firstly, the fast dynamics that typically characterizes those structures is absent from the data. Secondly, only half synodic rotation worth of data is needed to constrain the inversion problem for the whole coronal volume. As a result, coronal dynamics induced artifacts are reduced compared to previous DMT reconstructions. . The solution of the tomographic problem involves a very large sparse matrix. Such type of inversion problems are characterized by spurious high-frequency artifacts in the solution, which can be mitigated through *regularization* techniques (Frazin, 2000). In the case of DMT, all previous efforts used the 2D scheme implemented by Frazin, Vásquez, and Kamalabadi (2009), using a finite difference matrix operator to approximate angular derivatives in both latitude and longitude. Also new to the present work, is the implementation of an expanded 3D regularization scheme, which adds to the previous scheme a finite difference matrix operator to approximate radial derivatives. In this way, the tomographic inversion problem is performed penalizing nonphysical high-frequency artifacts in all three spatial directions. As a result, tomographic reconstructions behave more smoothly close to the radial boundaries of the computational grid when compared to previous reconstructions.

We summarize next the main aspects of DMT required for the analysis of this work. We refer the reader to Frazin, Vásquez, and Kamalabadi (2009) for a full description of the technique.

In a first step, the time series of EUV images is used to solve a solar rotational tomography (SRT) problem, for each EUV band independently. As a result, the 3D distribution of the so called *filter band emissivity* (FBE) is determined for each band separately. The FBE, an emissivity-type quantity, is defined as the wavelength integral of the coronal EUV spectral emissivity and the telescope's passband function of each EUV channel. Line-of-sight (LOS) integration of the FBE provides synthetic images that can be quantitatively compared to the real data in the time series. To find the FBE, the tomographic problem is posed as a global optimization problem in which the quadratic norm of the difference between all **pairs of synthetic and real images is minimized**.

In a second step, the FBE values obtained for all bands in each voxel **of the tomographic grid are used to constrain the determination of the LDEM which, as described in Section 1, describes the temperature distribution of the plasma within the individual voxel**. Specifically, at each tomographic voxel  $i$ , the FBE of the band  $k$  is related to the LDEM of the voxel according to

$$\text{FBE}_i^{(k)} = \int dT \text{LDEM}_i(T) \text{TRF}^{(k)}(T), \quad k = 1, \dots, K \quad (1)$$

where  $K$  is the number EUV bands, and  $\text{TRF}^{(k)}$  is the *temperature response function* of the  $j$ -th detector. The TRFs are here computed based on the (known) channel's passband times the coronal emissivity at that temperature (normalized by the squared electron density). The emissivity model used here is provided by the latest version of the CHIANTI atomic database and plasma emission model (Del Zanna *et al.*, 2015; Landi *et al.*, 2013).

Due to unresolved coronal dynamics, tomographic reconstructions exhibit negative values of the reconstructed FBE, or zero when the solution is constrained to positive values (Frazin, 2000; Frazin, Vásquez, and Kamalabadi, 2009). These non-reconstructed voxels are indicated as black voxels in the Carington maps of the reconstructed DENT results in Section 3.

Once the LDEM is determined at each voxel, **the LDEM-averaged squared electron density  $N_m^2$  and electron temperature  $T_m$  in the voxel can be computed** by taking its zeroth and first moments over temperature. More specifically, at the  $i$ -th voxel,

$$N_{m,i}^2 = \langle N_e^2 \rangle_i = \int dT \text{LDEM}_i(T), \quad (2)$$

$$T_{m,i} = \langle T_e \rangle_i = \frac{1}{\langle N_e^2 \rangle_i} \int dT T \text{LDEM}_i(T), \quad (3)$$

We define next a measure of the accuracy of the LDEM model to predict the tomographic FBEs in each voxel, as

$$R_i \equiv (1/K) \sum_{k=1}^K \left| 1 - \text{FBE}_{i,\text{syn}}^{(k)} / \text{FBE}_{i,\text{tom}}^{(k)} \right|, \quad (4)$$

---

being the average relative difference between the tomographic and the synthetic FBEs. The final product of DENT is in the form of 3D maps of the electron density and mean temperature. These relationships were derived in detail in Frazin, Vásquez, and Kamalabadi 2009 (see Appendix C).

## 2.2. AWSoM Simulations

NOTE: This section will summarize the AWSoM model. After a first version is written we will surely require some input from the Michigan friends. Points to cover:

- Data input. Link with the data input for DENT in terms of dates, etc. One paragraph.
- Main physical and technical aspects (grid in particular) of the model. One paragraph.
- Explain the artificially extended TR. One paragraph.
- What are the products of the model we care about in this paper. One paragraph.

In the transition region (TR), the plasma heats up and becomes less dense by several orders of magnitude over a short distance. Modeling this region realistically has a very high computational cost. For this reason, the model uses an artificially extended TR about  $\approx 0.05 R_{\odot}$  thick, as well as artificially large values for the electronic density and temperature as boundary conditions in  $r = 1 R_{\odot}$ . Consequently, model results below  $\approx 1.05 R_{\odot}$  were not taken into account in this article.

## 2.3. Tracing Results Along Magnetic Fieldlines

To determine the electron density and temperature along individual magnetic field lines, first both the thermodynamic results and the magnetic field obtained with the AWSoM model were interpolated into the DENT grid. Then, the geometry of the field lines is determined by numerical integration of the first order differential equations  $dr/B_r = r d\theta/B_{\theta} = r \sin(\theta) d\phi/B_{\phi}$ , both inwards and outwards, from the specified 3D coordinates of a starting point. In order to evenly sample the whole volume spanned by the DENT reconstructions, one starting point is selected at the center of each tomographic cell at 6 uniformly spaced heights, ranging from  $1.025$  to  $1.225 R_{\odot}$ , and every  $2^{\circ}$  in both latitude and longitude, for a total of 96,000 starting points.

For analysis purposes, the traced magnetic field lines are classified as open or closed according to their full geometry. Each closed field line is further classified as “small” or “large”, according to its coronal length  $L$  being respectively smaller or larger than the median value of the whole population, which is  $Md(L) \approx 0.5 R_{\odot}$  for both rotations. Finally, each closed magnetic field line is separated in its two “legs”, defined as the two segments that go from each of its two footpoints (i.e. their location at  $r = 1 R_{\odot}$ ) to its apex (i.e., the location of maximum height).

At this stage, DENT and AWSOM products can be traced along open and closed magnetic field lines. Once the field line geometry is computed in high spatial resolution, only one sample point per tomographic cell is kept (the median one). To each sample point, the results corresponding to the tomographic voxel where it is located are assigned to it. As a result, for each field line one data point per tomographic cell is obtained. This approach was firstly used by Huang *et al.* (2012) to study temperature structures in the solar minimum corona and by Nuevo *et al.* (2013) to expand that analysis to rotations with different level of activity.

For each open field line and for each closed field leg, an exponential fit was applied to the electron density data points and a linear fit applied to the electron temperature data points. For the DENT model the data points used were  $\sqrt{N_m^2(r)}$  and  $T_m(r)$ , and in case of the AWSOM models the data points used were  $N_e(r)$  and  $T_e(r)$ . The exponential and linear fit equations are described by

$$\sqrt{N_m^2} = N_0 \exp[-(h/\lambda_N) / (r/R_\odot)] \quad (5)$$

$$T_m = T_0 + m h \quad (6)$$

where  $h \equiv r - 1 R_\odot$  is the coronal height measured from the photosphere. In the electron density fit,  $\lambda_N [R_\odot]$  is the density scale height and  $N_0 [\text{cm}^{-3}]$  is the electron density at the footpoint ( $h = 0$ ) of the loop. In the electron temperature fit,  $m [\text{MK}/R_\odot]$  is the slope and  $T_0 [\text{MK}]$  is the electron temperature at the footpoint of the loop. The slope  $m$  is the radial gradient of the electron temperature along the loop, which we denote as  $m = \nabla_r T_m$  hereafter, being  $\nabla_r \equiv \mathbf{e}_r \cdot \nabla$  the radial derivative operator, where  $\mathbf{e}_r$  is the heliocentric radial unit vector.

In the case of the electron density, the fitted function corresponds to the isothermal hydrostatic equilibrium solution, allowing for variation of the solar gravitational acceleration with height. This choice of function provides a straightforward means to directly evaluate how compatible is the observed coronal thermodynamical state with the hydrostatic solution.

Coronal magnetic structures for which temperature increases/decreases with height (in the inner corona) were dubbed as “up”/“down” loops by Huang *et al.* (2012) and Nuevo *et al.* (2013), who first reported their presence by means of DENT studies. As speculated by the authors of those works, loops of type down can be expected if the heating deposition is strongly confined near the coronal base of a magnetic loop. Down loops were first predicted by Serio *et al.* (1981), and later on by Aschwanden and Schrijver (2002). In a recent study, Schiff and Cranmer (2016) reproduced both down and up loops by means of numerical simulations, using a 1D steady-state model and considering time-averaged heating rates.

NOTE: El párrafo que sigue describe un algoritmo para identificar y seleccionar piernas up/down. Es correcta la jerga de “confidence level” y el como se describe chi-squared test? Están bien mencionadas ambas cosas? Por ejemplo: confidence-level y confidence-interval, son dos cosas diferentes. Otro tema es: si entiendo bien el chi-squared utiliza los errores, correcto? Noten que modifiqué a errores porcentuales (mucho más claro) tal como se describen en las conclusiones (los

---

corregí un poco, aquí y allá), que los saqué de la Tabla 7, y re-escribí toda la frase (ver nuevo texto naranja), es correcta?. Ahora bien, son errores muy pequeños para cada celda, es poner demasiada fé en la tomografía :) Estos son los errores del valor mediano de  $T_m$ . Podemos discutirlo, pero creo que los errores por punto (es decir, la  $T_m$  de cada voxel) deben adjudicarse valores mayores. Quizá esto de paso hace que el chi-squared ralee menos?

To determine if a traced field line leg is of type up or down, we first determine the Pearson correlation coefficient  $\rho(T, r)$  between the DENT temperature  $T_m$  and the heliocentric height  $r$  data points. We then select field lines for which the temperature increases or decreases significantly with height by requiring  $|\rho(T, r)| > 0.5$ . We then measure the quality of the linear fit to the temperature-height data by means of a chi-squared test (Press *et al.*, 2002), and select legs for which the fit has a 90% confidence level. In this way, legs for which the DENT temperature does not show a significant variation with height, or the linear fit to temperature is good enough, are not considered in this analysis. Finally, selected legs are then classified as up or down according to if  $\rho(T, r) > +0.5$  or  $\rho(T, r) < -0.5$ , respectively. The linear fit allows characterization of the variation of  $T_m$  with height by means of a characteristic temperature gradient  $\nabla_r T_m$  [MK/R<sub>⊙</sub>] along each leg. **The chi-squared test to evaluate the quality of the fits considers the uncertainty level in the DENT products due to systematic sources (radiometric calibration and tomographic regularization), that Lloveras *et al.* (2017) estimated to be  $\Delta T_m \approx 6\%$  and  $\Delta \sqrt{N_m^2} \approx 3\%$ .** In summary, to be selected a leg must meet all three following conditions:

- i) The leg must go through at least five tomographic grid cells with reconstructed data, and there must be at least one data point in each third of the range of heights spanned by the leg. This requirement is set to ensure a reasonably spread sample of heights along the leg.
- ii) The DENT temperature and height data points must meet  $|\rho(T, r)| > 0.5$ .
- iii) The confidence level of both the exponential and linear fits must be larger than 90%.

To characterize the global thermodynamic state of the inner solar corona in distinct magnetic structures, the DENT and AWSOM results were traced along the magnetic field lines of the latter model. Based on the geometry and size of the loops, as well as on their thermodynamical properties, their legs were classified in four different types in this work:

- Type 0: closed-small-down with footpoints in the range  $|\text{latitude}| < 50^\circ$ .
- Type I: closed-small-up with footpoints in the range  $|\text{latitude}| < 50^\circ$ .
- Type II: closed-large-up with footpoints in the range  $|\text{latitude}| > 40^\circ$ .
- Type III: open with footpoint in the range  $|\text{latitude}| > 60^\circ$ .

In Section 3, the results of both the DENT and AWSOM models in the distinct magnetic structures are statistically analysed. As shown in Section 3.1 below, classification of legs from type 0 through II allows studying the streamer belt in three distinct, progressively outer layers.

## 2.4. Energy Input Flux

The high temperature of the corona requires heating mechanisms to compensate for the the losses. While the vast majority of the existing literature on coronal heating focuses on ARs, some studies have been dedicated to the heating of quiet-Sun regions. In particular, Mac Cormack *et al.* (2017) developed a new application of the DENT technique to estimate the energy input flux required at the base of quiet-Sun coronal loops to maintain them stable. The technique is based on tracing the DENT results along field lines of a global coronal magnetic model, just as described in the previous Section 2.3.

Consider a simple energy balance for each magnetic flux tube, in which the dominating losses of radiative power ( $E_r$ ) and thermal conduction power ( $E_c$ ) are compensated by a coronal heating power( $E_h$ ) (Aschwanden, 2004):

$$E_h(s) = E_r(s) + E_c(s), \quad (7)$$

where  $s$  is the position along the flux tube and the power quantities are in units of  $[\text{erg sec}^{-1} \text{ cm}^{-3}]$ .

The thermal conduction power  $E_c$  equals the divergence of the conductive heat flux  $F_c$ , i.e.  $E_c(s) = [1/A(s)] d[A(s) F_c(s)]/ds$ , where  $A(s)$  is the transversal area of the magnetic flux tube at position  $s$ . Under a quiescent solar corona plasma regime, the conductive flux is assumed to be dominated by the electron thermal conduction, described by the usual Spitzer model (Spitzer, 1962)

$$F_c(s) = -\kappa_0 T(s)^{5/2} \frac{dT}{ds}(s), \quad (8)$$

where  $\kappa_0 = 9.2 \times 10^{-7} \text{ erg sec}^{-1} \text{ K}^{-7/2}$  is the Spitzer thermal conductivity.

Radiative power depends on the amount of plasma in certain temperatures that can radiate. The model estimate it by integrating the squared density multiplied by a radiative loss function  $\Lambda(T)$ . This function depends on plasma temperature and is calculated by the atomic database and the plasma emission model from CHIANTI (Del Zanna *et al.*, 2015). Then, the expression for radiative power obtained is:

$$E_r = \int dT \text{LDEM}(T) \Lambda(T) \quad (9)$$

The energy balance given by Equation (7) is then integrated in the volume of any given coronal magnetic flux tube. Dividing the result by the flux tube area at the coronal base, and making use of the soleidonal conditon of the magnetic field, a field-line integrated version of that energy balance is found,

$$\phi_h = \phi_r + \phi_c. \quad (10)$$

where the line integrated flux quantities  $\phi_{r,c} [\text{erg sec}^{-1} \text{ cm}^{-2}]$  are given by (Mac Cormack *et al.*, 2017),



---


$$\phi_r = \left( \frac{B_0 B_L}{B_0 + B_L} \right) \int_0^L ds \frac{E_r(s)}{B(s)} \quad (11)$$

$$\phi_c = \left( \frac{B_0 F_{c,L} - B_L F_{c,0}}{B_0 + B_L} \right) \quad (12)$$

Note that, for any given field line, all quantities in these two expressions can be computed from the DENT and AWSOM models through Equations (8)-(9). Once computed, the quantity  $\phi_h$  can be calculated, which is the energy input flux required at the coronal base of each coronal field-line to maintain a stable coronal structure.

### 3. Results

#### 3.1. Tomographic Results

As described in Section 2.1, we carried out DENT reconstructions of the coronal structure for target rotations CR-2082 and CR-2208 using STEREO/EUVI and SDO/AIA data, respectively. Once the LDEM was determined for each rotation, the square root of the mean value of the electron density squared  $\sqrt{N_m^2}$  and the electron mean temperature  $T_m$  were computed at each voxel of the tomographic computational grid by means of Equations 2 and 3, and the measure  $R$  was calculated by means of Equation (4).

As an example, Figures 1 and 2 show latitude-longitude maps of DENT results for both rotations. Three different heights of interest are selected from the tomographic grid, providing also a detailed 3D view of the tomographic results: the lowest height of tomographic results ( $1.025 R_\odot$ ), the lowest height where the AWSOM results are fully consistent with coronal conditions ( $1.065 R_\odot$ ), and a middle height of the tomographic grid ( $1.105 R_\odot$ ). Black voxels correspond to non-reconstructed voxels (see Section 2.1). Thick-black curves indicate the open/closed boundaries of the magnetic field of the AWSOM model.

Both target rotations are highly axisymmetric, i.e. characterized by a high azimuthal symmetry. Rotation CR-2082 showed two small ARs (active regions), both near latitude  $+30^\circ$  and around longitudes  $50^\circ$  and  $120^\circ$ , respectively. Rotation CR-2208 showed two ARs, both near latitude  $+5^\circ$  and around longitudes  $140^\circ$  and  $300^\circ$ , respectively.

The magnetically open and closed regions of the AWSOM model are associated to CHs and the equatorial streamer belt, respectively. Consistently with that, the location of the open/closed boundaries derived from the respective AWSOM model quite accurately match the regions of the DENT maps which exhibit the strongest latitudinal gradient of both the electron density and temperature.

Figures 1 and 2 show that the DENT reconstruction of the streamer belt is characterized by relatively larger values of density and temperature in comparison to the CHs. They also show that the streamer belt region of CR-2082 was denser and colder than that of CR-2208. In the case of CR-2082, which belongs

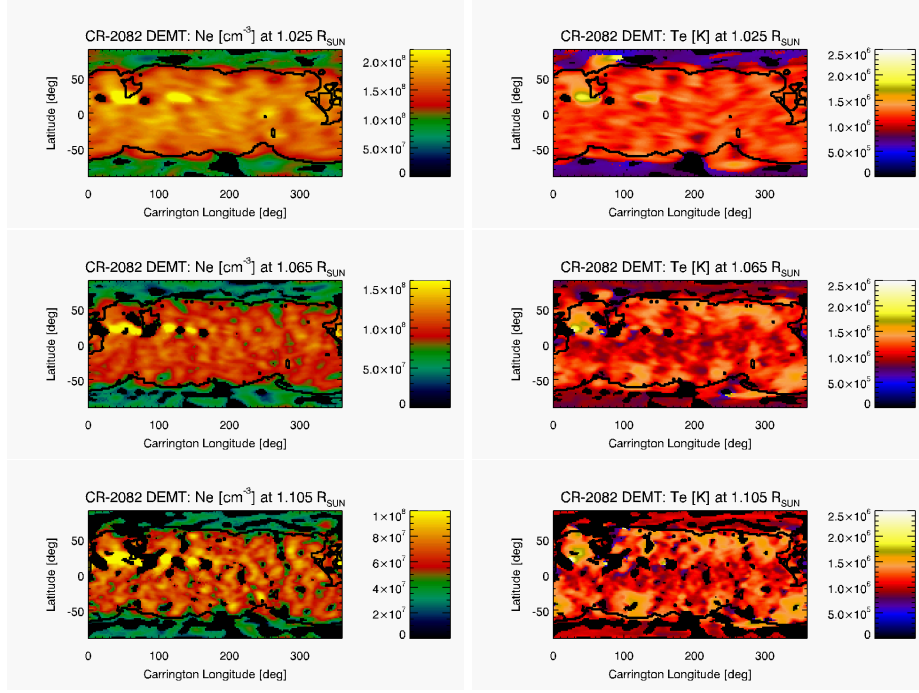


**Figure 1.** Carrington maps of DMT products  $\sqrt{N_m^2}$  (left panels) and  $T_m$  (right panels) for CR-2082. Top, middle and bottom panels show the results at three heliocentric heights, 1.025, 1.065 and 1.105  $R_{\odot}$  respectively. Black voxels correspond to non-reconstructed regions (see text in Section 3.1) and thick-black curves indicate the open/closed boundaries.

to the deep minimum epoch between SCs 24 and 25, the low latitudes of the streamer belt are characterized by lower electron temperature than in its mid-latitudes. A similar behavior is seen in CR-2208, belonging to the declining phase of SC 25, but having a somewhat less axisymmetric structure this characteristic is not so obvious. This thermodynamic structure of the streamer have been reported for other solar minimum rotations in previous DMT works (Lloveras *et al.*, 2017; Nuevo *et al.*, 2013; Vásquez, Frazin, and Manchester, 2010).

For both target rotations, Figure 3 shows latitude-longitude maps of the DMT measure  $R$  defined by Equation (4), at the same three heights shown in Figures 2 and 3. In most of the coronal volume of the DMT grid the agreement between the tomographic and synthetic FBEs is  $\lesssim 1\%$ . The notable exception is to be found in the CHs of the target rotation analysed based on AIA data. A similar results was found in the two existing DMT works based on data provided by the AIA instrument (Nuevo *et al.*, 2015; Mac Cormack *et al.*, 2017). This point is further discussed below.

To characterize the DMT results in different magnetic structures, we traced  $\sqrt{N_m^2}$  and  $T_m$  along the magnetic field lines of the AWSoM model. For both rotations, all field lines that meet the criteria listed in Section 2.3 were selected. For each field line, the data points of electron density and electron mean tem-

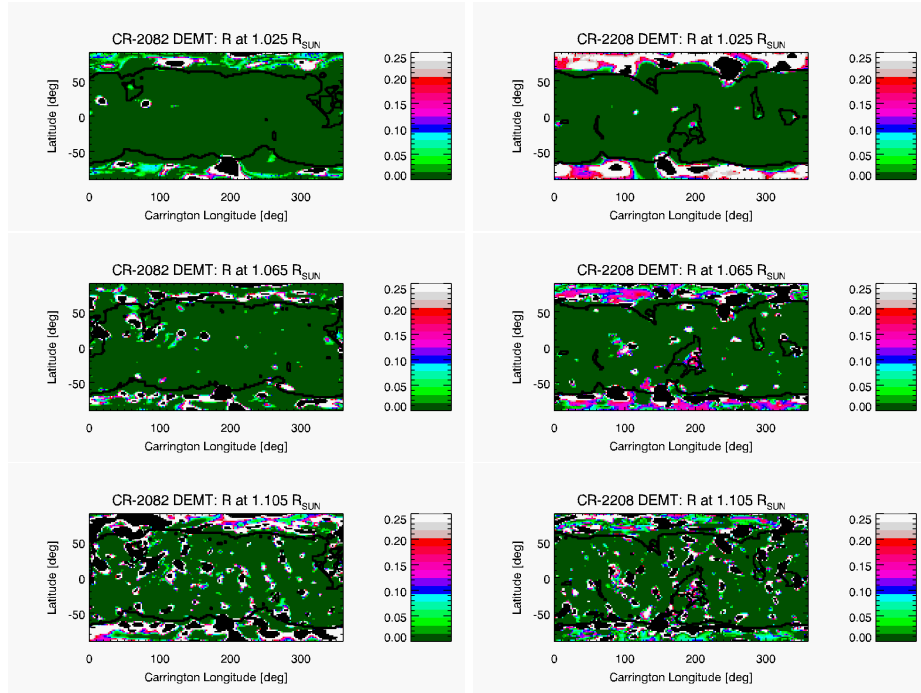


**Figure 2.** Same as Figure 1 but for CR-2208.

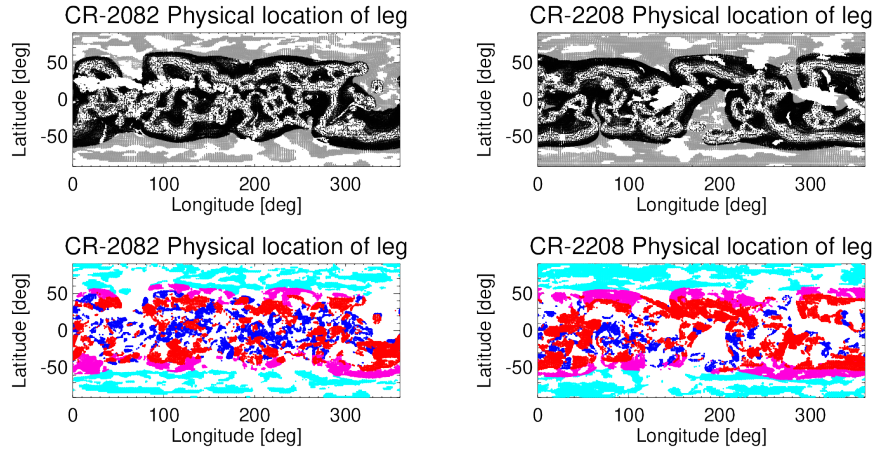
perature as a function of height were fitted to the Equations 5 and 6. As a result, the electron density  $N_0(r = 1.0 R_\odot)$  and scale height  $\lambda_N$  were computed for each leg, as well as the temperature gradient  $\nabla_r T_m$ , and the height-averaged (along the leg) electron temperature  $\langle T_m \rangle$ .

For both target rotations, the top panels of Figure 4 show the latitude-longitude location (at heliocentric height  $r = 1.105 R_\odot$ ) of all traced field line legs for which criterion (i) of Section 2.3 is met. Open legs are indicated in gray color and closed ones in black color. For each leg, the fits to tomographic temperature and density were applied, as given by Equations (5)-(6). Considering the DEMT data points and the resulting fits along each leg, the bottom panels of Figure 4 show the latitude-longitude location of the subset for which also both criteria (ii) and (iii) of Section 2.3 are met. Using a four-color code, type 0, I, II and III legs are shown in blue, red, magenta and cyan color, respectively. Of the  $\approx 48000$  legs selected for CR-2082, 21% are type 0, 31% are type I, 22% are type II and 26% type III. On the other hand, of the  $\approx 57000$  legs selected for CR-2208, 9% are type 0, 36% are type I, 26% are type II and 29% type III.

Type 0 (small down) legs mainly populate the equatorial latitudes. This kind of structure was originally found by Huang *et al.* (2012), and their existence was shown to be anti-correlated with the solar activity level around the solar minimum between SCs 24 and 25 by Nuevo *et al.* (2013). Later on, Lloveras *et al.* (2017) showed that equatorial down loops in streamers were also to be found in the deep minimum between SCs 23 and 24. Here, we verify the existence of this

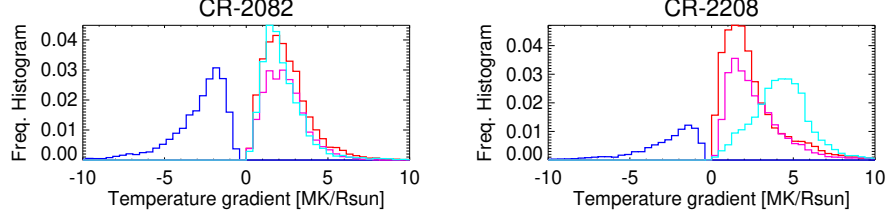


**Figure 3.** Carrington maps of the measure  $R$  defined by Equation (4), for CR-2082 (left panels) and CR-2208 (right panels), at heights 1.025, 1.065 and  $1.105 R_{\odot}$ , from top to bottom.



**Figure 4.** *Top panels:* latitude-longitude location at heliocentric height  $r = 1.105 R_{\odot}$  of all open (grey color) and closed (black color) traced field line legs for which criterion (i) of Section 2.3 is met, for both CR2082 (left) and CR2208 (right). *Bottom panels:* latitude-longitude location of the subset for which also both criteria (ii) and (iii) of Section 2.3 are met. The location of type 0, I, II and III legs is shown in blue, red, magenta and cyan color, respectively.

type of structure for the two target rotations. The relatively smaller population of down loops seen in CR-2208, as compared to CR-2082, is consistent with the aforementioned results by Nuevo *et al.* (2013). Type I (small up) mainly populate the mid-latitudes, while type II (large up) legs are mostly very large trans-equatorial field lines forming the envelope of the streamer belt. Finally, type III (open) legs populate of course the CHs.



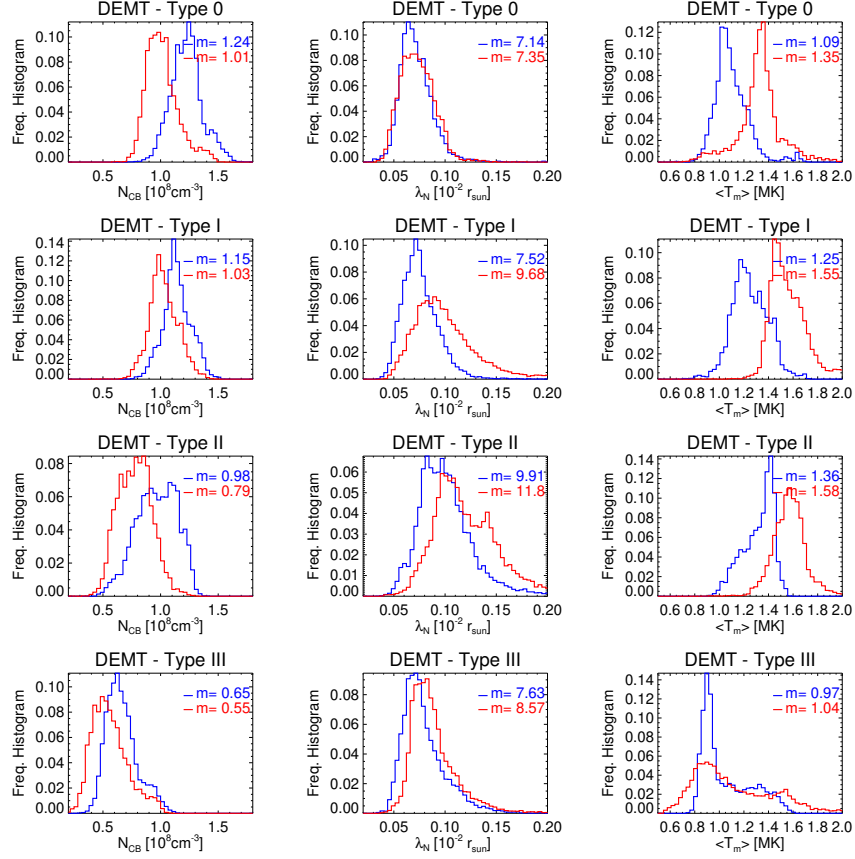
**Figure 5.** Frequency histograms of the temperature radial gradient for the four types of legs in Figure 4 (using the same color code) for CR-2082 (left panel) and CR-2208 (right panel).

Figure 5 shows frequency histograms (normalized to the total amount of selected field lines) of the temperature radial gradient ( $\nabla_r T_m$ ) for legs of type 0, I, II and III. The lack of population around values close to zero is due to the requirement  $|\rho(T, r)| > 0.5$  which discards quasi-isothermal legs. For both rotations, the median value of the temperature radial gradient is  $\text{Md}(\nabla_r T_m) \approx -2.5$ ,  $-2.3$  and  $-2.4$  MK/R $_{\odot}$  for legs of type 0, I and II, respectively.

The notable difference between both rotations is the characteristic value  $\text{Md}(\nabla_r T_m) \approx +4.5$  MK/R $_{\odot}$  for legs of type III for CR-2208. This is related to the much larger  $R$  score for the DMT results along CH legs for CR-2208. In this case, DMT performs poorly in modeling a LDEM that predicts the tomographic FBEs with reasonable accuracy. Indeed, visual inspection of the DMT temperature maps for CR-2208 in Figure 3, reveals that in most of the CH region the result for  $T_m$  below height  $1.105 R_{\odot}$  is quite uniform and artificially low. As it turns out, around and above height this height the score  $R$  is lower and the temperature results are more reliable. As a result, the temperature gradient along these legs is artificially larger, with the linear fit trying to simultaneously fit the artificially low values of  $T_m$  at lower heights. In general, the DMT results in the CH region based on AIA data are thus much less reliable than in the rest of the analysis. We will return to this point in the conclusion section.

For both rotations, Figure 6 shows, in a statistical fashion, the DMT results traced along field lines discriminated by field line type. From top to bottom results are shown for type 0 to type III field lines, respectively. From left to right the panels show the statistical distribution of  $N_{CB} \equiv \sqrt{N_m^2}(r = 1.055)$  (the lowest height where the AWSOM results are consistent with coronal conditions),  $\lambda_N$  and  $\langle T_m \rangle$ , with the median value  $m$  indicated in each plot.

Table 1 summarizes a quantitative comparative analysis between the results of the two target rotations. For CR-2082 quantities are expressed as absolute values, while for CR-2208 they are informed as a percentual variation relative to the corresponding results for CR-2082. The following major results, both concerning



**Figure 6.** Statistical distribution of DENT results for rotations CR-2082 (blue) and CR-2208 (red) traced along legs of type 0, I, II and III (from top to bottom), as defined in Section 2.3. From left to right: electron density  $N_{CB} \equiv \sqrt{N_m^2}(r = 1.055 R_{\odot})$ , electron density scale height  $\lambda_N$ , and loop-averaged temperature  $\langle T_m \rangle$ . In each panel the median value  $m$  is indicated.

the structure of each rotation individually as well as their comparison, can be drawn.

Throughout the magnetically closed region of both rotations, type 0, I and II legs, associated to increasingly outer regions of the equatorial streamer belt, progressively exhibit decreasing coronal base density, increasing density scale height, and increasing electron temperature. In both rotations also, type III field lines in the CHs are characterized by sub-MK temperatures, and electron density values of order  $\approx 1/2$  of those observed for the type 0 and type I lines in the core of the equatorial streamer.

A comparison of the results between the two rotations shows that, compared to CR-2082, target rotation CR-2208 was characterized by  $\approx 10 - 20\%$  lower values of the electron density at the coronal base,  $\approx 5 - 30\%$  larger values of density scale height, and  $\approx 5 - 25\%$  larger values of the electron temperature.

**Table 1.** Median value (indicated as “Md”) of the statistical distribution of  $N_{CB}$ ,  $\lambda_N$ , and  $\langle T_m \rangle$  for each coronal type of lines defined in Section 2.3. For CR-2082 values are expressed in absolute terms, while for CR-2208 they are informed as a percentual variation relative to the CR-2082 value.

Type	Md( $N_{CB}$ ) [ $10^8 \text{ cm}^{-3}$ ]	Md( $\lambda_N$ ) [ $10^{-2} \text{ R}_\odot$ ]	Md( $\langle T_m \rangle$ ) [MK]
0	1.24 (-19%)	<b>7.1</b> (+ 3%)	1.09 (+24%)
I	1.15 (-10%)	7.5 (+29%)	1.25 (+24%)
II	0.98 (-20%)	9.9 (+19%)	1.36 (+16%)
III	0.65 (-15%)	7.6 (+12%)	0.97 (+ 7%)

To analyze the loop-integrated energy flux quantities introduced in Section 2.3, we selected closed loops for which both legs have the same sign of the radial gradient of the electron temperature  $\nabla_r T_m$ . In this way, according to the classification of both its legs, each given loop was classified as of type 0 (small down loop), I (small up loop), or II (large up loop). For both target rotations, and for loops of type 0, I and II, Figure 7 shows the frequency histogram of the loop-integrated energy flux quantities  $\phi_r$ ,  $\phi_c$  and  $\phi_h$  in blue, green and red color, respectively.

For both rotations, the value of the loop-integrated radiative power  $E_r$ , measured by the quantity  $\phi_r$ , is largest for loops of type 0. This is due to  $E_r \propto N_e^2 \Lambda(T_e)$ , with both factors contributing to maximize  $E_r$  for loops of type 0. As shown in Figure 6 and Table 1, loops of type 0 are characterized by the largest values of electron density. Also, in the range of sensitivity of the EUVI and AIA instruments, namely 0.5–3.0 MK (Nuevo *et al.*, 2015), the radiative loss function  $\Lambda(T)$  has a local maximum at  $T_c \approx 1$  MK. According to Figure 6, loops of type 0, I and II are characterized by values of temperature that are progressively larger and farther from the value  $T_c$ , for both rotations.

The sign of the quantity  $\phi_c$  depends on that of the conductive flux  $F_c$ . Equations (8) and (12) imply that down loops (type 0) and up loops (type I and II) are characterized by  $\phi_c < 0$  and  $\phi_c > 0$ , respectively, as verified in Figure 7.

Adding the radiative and conductive terms, the characteristic energy input flux at the coronal base is in the range  $\phi_h \approx 0.5 - 1.5 \times 10^5 \text{ erg cm}^{-2} \text{ s}^{-1}$ , depending on the rotation and the type of loop, matching the values reported by Mac Cormack *et al.* (2017). Note that for type 0 loops there is a marginal population characterized by the unphysical result  $\phi_h < 0$ . As shown by Mac Cormack *et al.* (2017), this affects only the smallest sized loops of the type 0, and it is most probably due to the limited temperature sensitivity of the instrumental passbands. The radiative loss term is here calculated based on plasma emission detected by three coronal bands of EUVI or AIA. Though accounting for most of the coronal plasma, there surely is additional emission out of the instrumental sensitivity range. As a result, the positive term  $\phi_r$  is most likely underestimated, leading to values  $\phi_h < 0$  in loops of type 0, being characterized by  $\phi_c < 0$ .

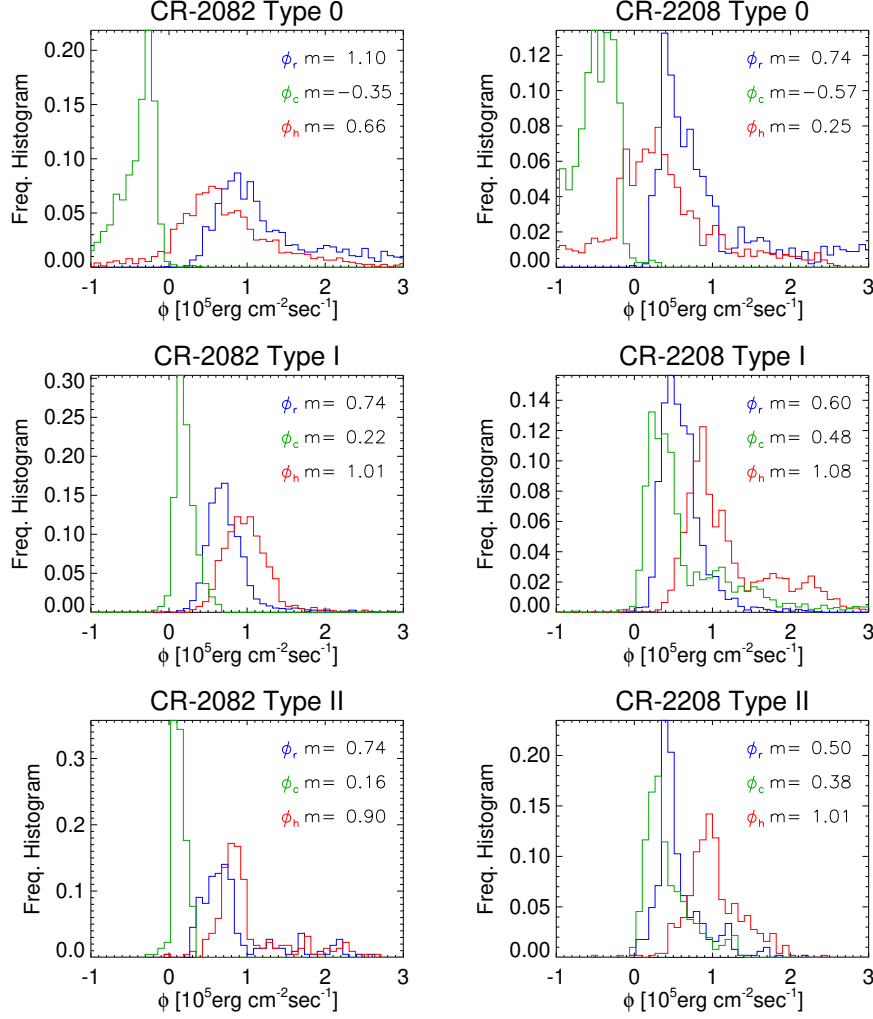


**Figure 7.** Statistical results of the loop-integrated energy flux quantities  $\phi_r$ ,  $\phi_c$ , and  $\phi_h$  in colors blue, red and green, respectively for CR-2082 (left) and CR-2208 (right). From top to bottom, panels show the results for loops of type 0, I and II, which are loops for which both legs meet the criteria from Section 2.3.

### 3.2. Comparison of the DGMT and AWSoM Models

For both target rotations, Figures 8 and 9 show latitude-longitude maps of the AWSoM electron density and temperature. Maps are shown at the same three heights selected for visualization of the DGMT results in Figures 1 and 2. Thick-black curves indicate the magnetic open/closed boundaries based on the magnetic field of the AWSoM model. Visual inspection of these maps shows that the AWSoM model for both rotations is highly axisymmetric, as the tomographic model.



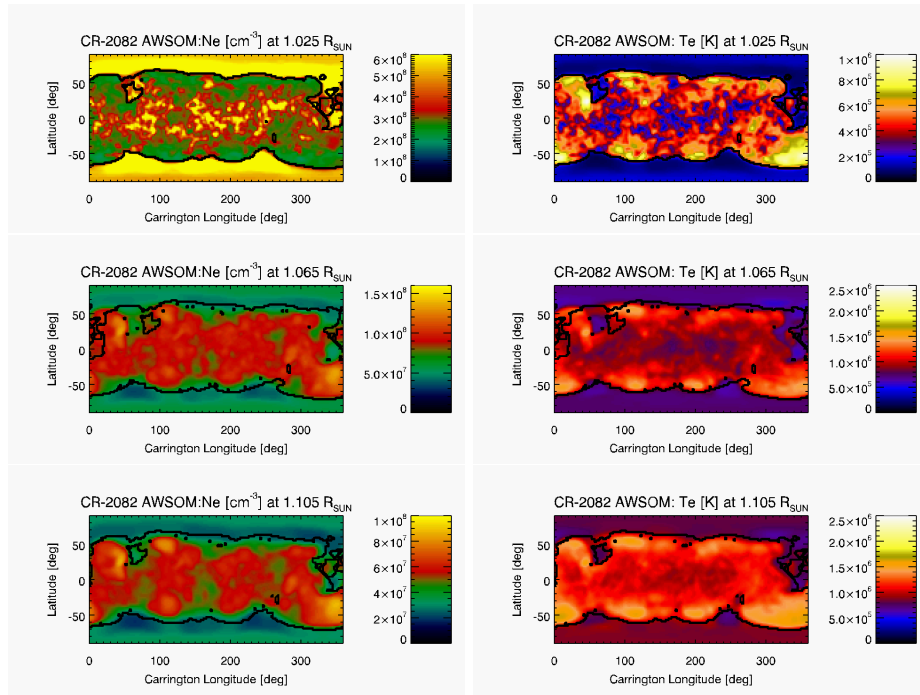


**Figure 8.** Carrington maps of density (left panels) and temperature (right panels) obtained with AWSOM model for the same three heights shown in Figure 1.

As described in Section 2.2, the AWSOM model includes an artificially thick TR, achieving coronal conditions above height  $\approx 1.06 R_{\odot}$ . Indeed, the top panels in Figures 8 and 9, at height  $1.025 R_{\odot}$ , clearly do not represent coronal conditions (although we include them here for completeness). When compared to DMT results (Figures 1 and 2), the latitude-longitude maps of the AWSOM model for heights  $1.065$  and  $1.105 R_{\odot}$  capture well the denser and hotter equatorial streamer belt surrounded by the less dense and colder CHs. Furthermore, for both target rotations, the temperature maps show the low latitudes of the equatorial streamer belt to be characterized by lower temperatures than its mid-latitudes, as also seen in the DMT results. The latitude-longitude maps of the AWSOM and DMT results are shown in the same units and scales, so that a visual comparison among them already reveals similar values of electron density and temperature in both models.

Being highly axisymmetric target rotations, the longitude-averaged latitudinal variation of the results of both models is an informative way to compare their large-scale structure. Such comparison is shown in Figure 10 at height  $1.105 R_{\odot}$ , with top panels comparing electron density and lower panels electron temperature. In these longitude-averaged profiles, longitudes containing ARs or low latitude CHs were excluded. In each panel the averaged latitudinal variation for the DMT model is shown in solid-line style, while the result for the AWSOM model is shown in dashed-line style. Left panels show the comparison for CR-2082

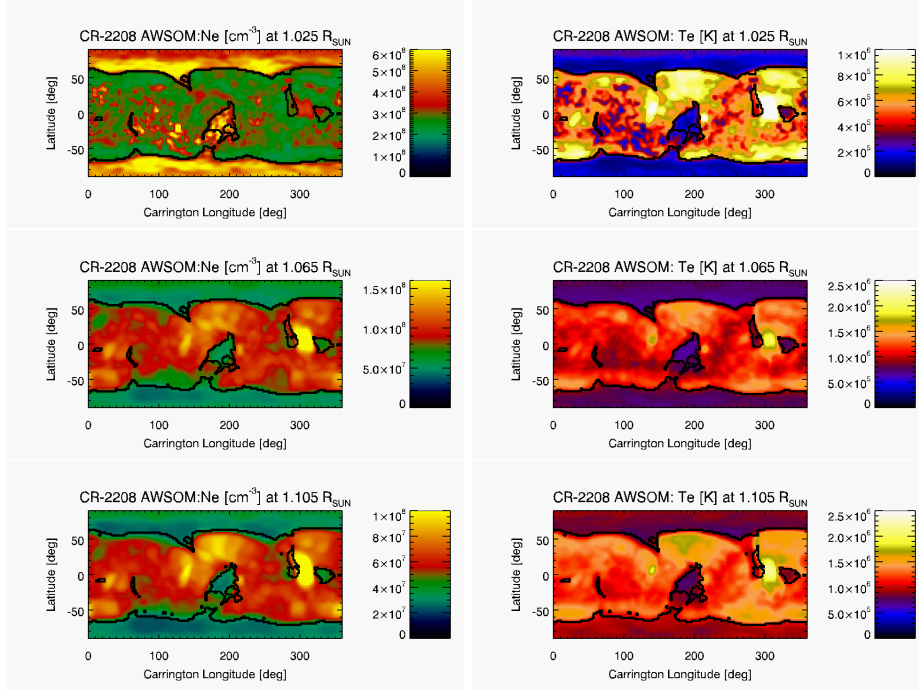


**Figure 9.** Same as Figure 9 for CR-2208.

(in blue) and right panels for CR-2208 (in red). In each panel the vertical black lines denote the corresponding longitude-averaged latitude of the open-close boundary in both hemispheres.

Several details from Figure 10 are worth being highlighted. Firstly, for CR-2082 the electron density of both models agree within  $\approx 20\%$  at all latitudes, and for CR-2208 the agreement is within  $\approx 5\%$ . In the case of the electron temperature both models agree within  $\approx 10-15\%$  at all latitudes for both target rotations. Secondly, for both target rotations, and for both models, these plots clearly show the relatively lower temperatures characterising the low-latitudes of the equatorial streamer belt compared to its mid-latitudes. Thirdly, for both target rotations, the latitude of the open/close magnetic boundary in both hemispheres matches the location of the strongest latitudinal gradient of the DMT electron density. Note this is not the case for the AWSOM model, that shows a minimum density at the open/closed boundary. Last, note that the DMT electron density decreases from the open/close boundary towards the poles (in both hemispheres of the two target rotations), while the AWSOM model shows the opposite trend.

To characterize the results of the AWSOM model in distinct magnetic structures, its results for electron density and temperature were traced along its magnetic field lines. For each field line leg, the results were then fit to Equations (5) and (6), considering only data points above heliocentric height  $1.055 R_{\odot}$ . We then classified the traced legs into types I, II and III, according to the criteria

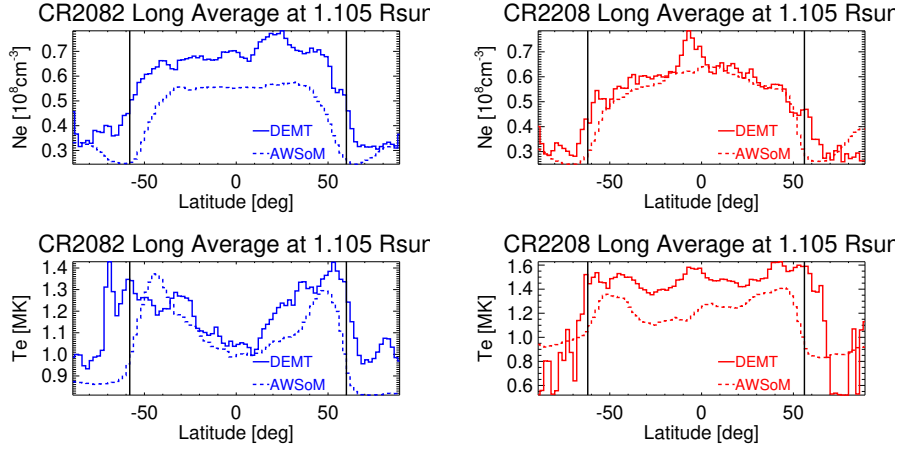


**Figure 10.** Longitude-averaged latitudinal dependence of the electron density (top) and temperature (bottom) for DMT (blue) and AWSoM (red) results at  $1.105 R_{\odot}$ . The left (right) panels correspond to CR-2082 (CR2208). The vertical black line indicates the longitude-averaged latitudes of the open/close magnetic boundary in both hemispheres.

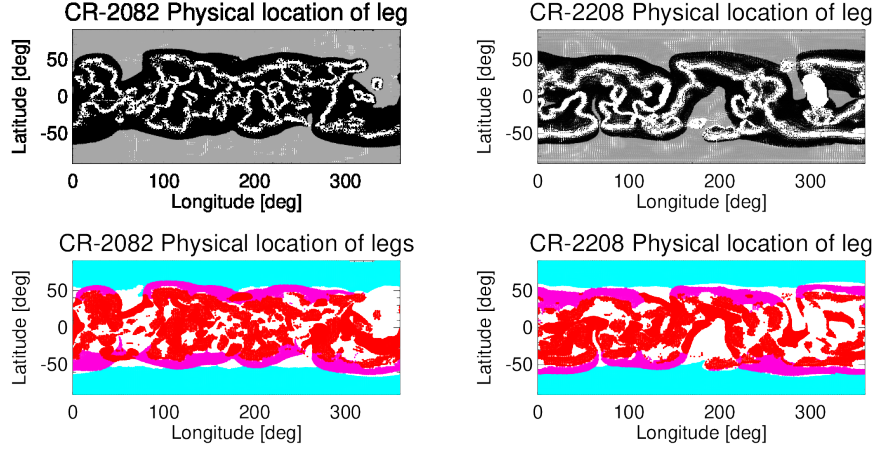


**Figure 11.** Same as Figure 4, but using the density and temperature of the AWSoM model to classify its legs in types I, II and III. The model does not exhibit legs of type 0.

described in Section 2.3. Legs of type 0 are not included for AWSoM, as in its current implementation it can not simulate down loops, a point we will discuss in the next section.

For both target rotations, the top panels of Figure 11 show the latitude-longitude location (at heliocentric height  $1.105 R_{\odot}$ ) of all traced field line legs for which criterion (i) of Section 2.3 is met. That criterion is adapted here, requiring that at least five voxels of the tomographic grid are threaded by the leg. Open legs are indicated in gray color and closed ones in black color. For each leg, the

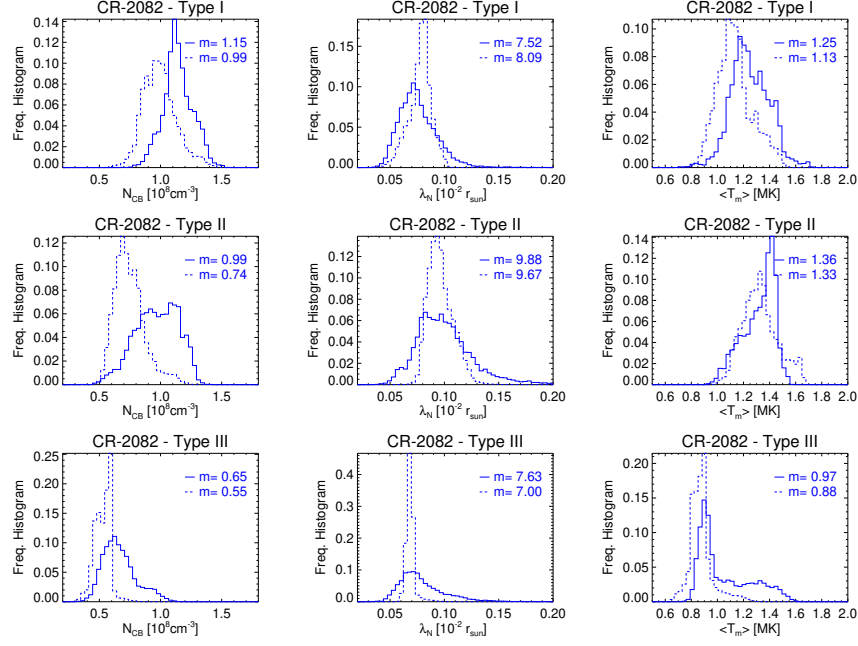


**Figure 12.** Statistical distribution of the results of the DENT (solid line-style) and AWSOM (dashed-line-style) models traced along legs of type I, II and III (from top to bottom), as defined in Section 2.3. From left to right: electron density at the lowest coronal height of the AWSOM model  $N_{CB}(r = 1.055 R_{\odot})$ , electron density scale height  $\lambda_N$ , and leg-averaged electron temperature  $\langle T_m \rangle$ . In each panel the median values  $m$  are indicated.

fits to tomographic temperature and density were applied, as given by Equations 5 and 6. Considering the AWSOM data points and the resulting fits along each leg, the bottom panels of Figure 11 show the latitude-longitude location of the subset for which also both criteria (ii) and (iii) of Section 2.3 are met. Using a three-color code, type I, II and III legs are shown in red, magenta and cyan color, respectively. This figure is to be compared with the corresponding Figure 4 for DENT results. It is readily seen that the AWSOM maps are more populated than those of DENT. This is due to the 3D MHD model having electron density and temperature fields spatially smoother than those of DENT.

For target rotation CR-2082, Figure 12 shows the statistical distribution of the results of the DENT (solid line-style) and AWSOM (dashed line-style) models traced along legs of type I, II and III (from top to bottom), as defined in Section 2.3. From left to right: electron density at the lowest coronal height of the AWSOM model  $N_{CB} \equiv N_e(r = 1.055 R_{\odot})$ , electron density scale height  $\lambda_N$ , and leg-averaged electron temperature  $\langle T_m \rangle$ . In each panel the median values  $m$  are indicated. Figure 13 shows the same analysis for target rotation CR-2208.

For the two target rotations, Table 2 summarizes a quantitative comparative analysis between the results of the DENT and AWSOM models based on the results shown in Figures 12 and 13. The DENT results are expressed as absolute

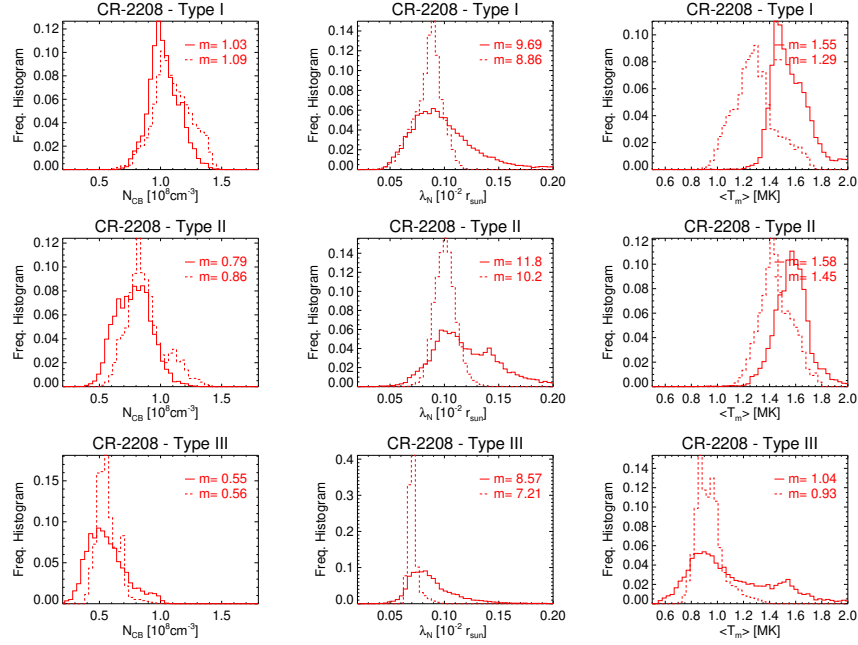


**Figure 13.** Same as Figure 12 for CR-2208.

values, while the ASWSOM results are informed as a percentual variation relative to the corresponding result for DGMT. The following major results can be drawn.

For target rotation CR-2082, the median value of the electron density  $N_{CB}$  of both models agree within  $\approx 10 - 25\%$ , depending of the type of leg, while the median value of the scale height  $\lambda_N$  agree within  $\approx 10\%$ . The leg-averaged electron temperature  $\langle T_m \rangle$  of both models also agree within 10%. For target rotation CR-2208 the agreement of the median value of  $N_{CB}$  and  $\lambda_N$  of both models is within 5%, while median values of  $\langle T_m \rangle$  agree within 15%. These detailed results informed per magnetic structure are fully consistent with the large-scale comparison provided in Figure 10.

Finally, to provide a graphical comparison of both models across the full range of heliocentric heights covered by the DGMT results, Figure 14 shows the average fits of  $N_e(r)$  and  $T_e(r)$  for legs of type I (red), II (magenta), and III (cyan) for both target rotations. In each panel the DGMT and ASWSOM results are plotted in solid and dashed linestyles, respectively.

As discussed above, Figure 10 shows that the longitude-averaged latitudinal profile of the DGMT electron density in the CHs decreases towards the poles. Figure 15 below shows the longitude-averaged ASWSOM radial wind speed  $V_r$  at  $6 R_\odot$ , where all field lines are open. The heliocentric current sheet (HCS) location is indicated by the minimum of the speed curve. For each rotation, all velocity data points to the south of the HCS position map down to the southern CH in Figures 10. Similarly, all velocity data points to the north of the HCS position map down to the northern CH in Figures 10. This clearly shows

**Table 2.** Median value (indicated as “Md”) of the statistical distribution of  $N_{CB}$ ,  $\lambda_N$ , and  $\langle T_m \rangle$  for each coronal type of lines defined in Section 2.3. DENT values are expressed in absolute terms, while AWSoM results are informed as a percentual variation relative to the corresponding DENT value.

Type	Md( $N_{CB}$ ) [ $10^8 \text{ cm}^{-3}$ ]	Md( $\lambda_N$ ) [ $10^{-2} R_\odot$ ]	Md( $\langle T_m \rangle$ ) [MK]
CR-2082			
I	1.15 (-14%)	7.5 (+ 8%)	1.25 (-10%)
II	0.99 (-25%)	9.9 (- 2%)	1.36 (- 2%)
III	0.65 (-15%)	7.6 (- 8%)	0.97 (- 9%)
CR-2208			
I	1.03 (+ 6%)	9.7 (- 8%)	1.55 (- 17%)
II	0.79 (+ 9%)	11.8 (-14%)	1.58 (- 8%)
III	0.55 (+ 2%)	8.6 (-16%)	1.04 (- 11%)

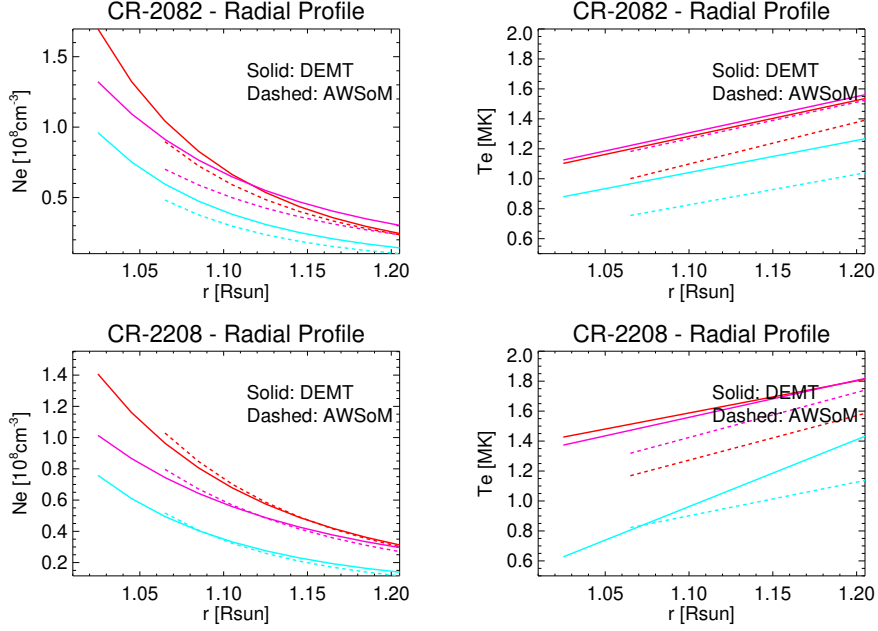


**Figure 14.** Average fits to  $N_e(r)$  (left panels) and  $T_e(r)$  (right panels) for legs of type I (red), II (magenta), and III (cyan), for CR-2082 (top panels) and CR-2208 (bottom panels). Solid lines correspond to DENT results while dashed lines correspond to AWSoM results.

an anti-correlation between the DENT electron density at low heights and the AWSoM wind speed at larger heights.

NOTE: We could quantify the anti-correlation between the AWSoM terminal speed and the DENT electron density at the coronal base in the following fashion. We can set up starting points at, say,  $20 R_{\odot}$ , every one degree, both in latitude and longitude. This would mean setting up  $180 \times 360$  starting points. We trace then the (open) field lines from each of those starting points down to  $1.0 R_{\odot}$  to find out the DENT results at those lower heights for each field line. Now, to do this we need to develop some codes and have no time for this paper. We can postpone it for a next effort, or... Chip: do you think you could do this with your present tools? Do you think it is interesting? I think so. Our submission deadline is end-of-January.

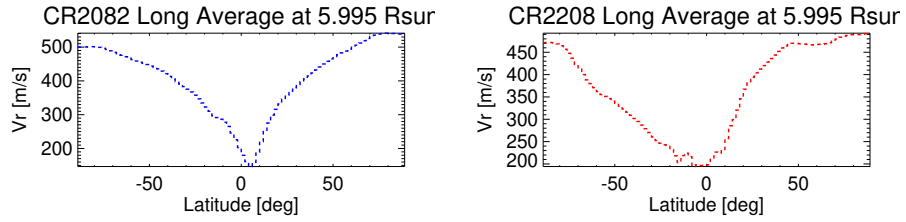


**Figure 15.** Longitude-averaged latitudinal dependence of the AWSoM model wind speed at  $6.0 R_{\odot}$  for CR2082 (left panel) and CR2208 (right panel). NOTE: (by Albert): Even if this is not yet the terminal speed, it is a pretty high height, and one can already see the transition from FAST to SLOW speed in the model, where the absolute minimum indicates the location of the HCS at this height. I believe it is interesting to compare these two curves with Figure 10. Note that while in this Figure all latitudes are magnetically open, in Figure 10 only the part at latitudes larger than the vertical black lines are open. Note that DENT shows that in the open low corona  $N_e$  decreases from the O/C boundary towards the poles, anti-correlating with the AWSoM terminal speed, which is nice. In order to quantify this anti-correlation we need to trace the terminal speed and the DENT  $N_e$ , which we may need to do with the help of Chip and Nishtha. Chip, we can discuss this idea over Skype after Xmas if you are around.

#### 4. Discussion and Conclusions

NOTE: Propongo que Diego escriba una primer sección limpia, ordenada. Lo que vos mandarías al Solar Physics, sin asteriscos ni nada raro. Expresate con párrafos limpios. Si querés destacar algo para discutir ponelo como una nota en rojo al final del párrafo correspondiente, no en el medio de los mismos. Yo creo que esto debe estructurarse así:

- i) Un párrafo (breve) de que se hizo, esto contextualiza.
- ii) Dos o tres párrafos sobre los resultados 3.1. Esto es: resultados per se de cada rotación y como comparan (mencionando el tema incertezas). Estructura 3D del streamer en CAPAS, revelada observacionalmente en forma global por DENT, esto incluye UP/DOWN loops. Explicar que con AIA no andamos bien en CHs. O sí? Energía.
- iii) Uno o dos párrafos sobre los resultados 3.2. Como compara AWSoM con DENT. En forma breve. Vale la pena explicar que DOWN loops no se puede.



- iv) Luego un párrafo sobre next steps. Esto puede incluir nuevas cosas con AIA-4, el Eclipse, otras rotaciones de mayor intensidad.

NOTE: Este párrafo que sigue es de Albert. Algo así debe ir incluído dentro de la parte que refiere a 3.1. Creo que hay que corregir números a la luz de los análisis finales. Creo que los números de cuanto más frío o caliente, etc, deben ser corregidos a la luz de la nueva Tabla 1.

In comparing the DENT results obtained for the two selected targets, it is important to bear in mind they rely on data provided by two different instruments: AIA and EUVI. In order to quantify the systematic difference of the DENT products based on both instruments, Nuevo *et al.* (2015), who were the first to apply DENT to AIA data, analysed a single target using both instruments independently. They found that while the density product is essentially equal, the temperature product of DENT based on AIA data is systematically 8% larger than the one based on EUVI data, i.e.  $T_m^{(AIA)}/T_m^{(EUVI)} \approx 1.08$ . Considering such correction, Figure 6 and Table 1 indicate that CR-2208 was  $\approx 10 - 15\%$  hotter than CR-2082 throughout the streamer belt region. As for the electron density products, CR-2208 was found to be  $\approx 15 - 20\%$  less dense than CR-2082 throughout the streamer belt region. These systematic differences are beyond the uncertainty level in the DENT products due to systematic sources (radio-metric calibration and tomographic regularization), that Lloveras *et al.* (2017) estimated to be  $\Delta T_m \approx 6\%$  and  $\Delta \sqrt{N_m^2} \approx 3\%$ .

NOTE: El texto hasta el final son de Diego. Algunos se pueden ir, otros pueden servir de semilla para construir las distintas partes de la Sección.

\*We found down legs in the DENT reconstructions mainly in the equatorial latitudes, being a greater quantity and better distribution along longitudes in CR-2082 than in CR-2208. Nuevo *et al.* (2013) showed a decrease in the amount of down loops as the solar activity increases, which is consistent with the results shown in this article.

\*We can see, on type 0 loops, a median value of energy input flux ( $\phi_h$ ) for CR-2082 twice bigger than CR-2208. In both rotations this magnitude has negative values, this can refer to some loops where loop-integrated radiative flux ( $\phi_r$ ) is too small in comparison with the larger gradients of negative conductive flux ( $\phi_c$ ), resulting in negative energy input flux.

This effect can be due a subestimation of the density present in the loop or the limited range of temperature used to reconstruct tomographic parameters, that can affect the compute of radiative power. Nevertheless, this population represent lower than the **ALGÚN PORCENTAJE%** of total population in both cases.

Consistent that the density in CR-2082 was higher, the  $\phi_r$  was also higher. In both rotations the magnitudes in the temperature gradients are similar, but the temperatures in CR-2208 were consistently higher at all heights, resulting in a larger  $\phi_c$  in module. This results are in agree with the observations of Mac Cormack *et al.* (2017).

**THE AR of CR-2082 wasn't well modeled by AWSOM.**

In both rotations, AWSOM and DENT results shows same thermodynamic structures along latitude and longitude with very comparable values between  $1.055 - 1.25 R_\odot$



Figure 12 and Table 2 indicate that AWSoM reconstruction of CR-2082 was found to be less dense  $\approx 11 - 22\%$  and colder  $\approx 5 - 10\%$ .

Both reconstructions of CR-2208 reconstructed the ARs with very similar values and in almost the same latitude-longitude location. Figure 13 and Table 2 indicate that AWSoM reconstruction of CR-2208 was found to be denser  $\approx 0 - 10\%$  and colder  $\approx 10 - 15\%$ .

CR-2208 was  $\approx 10 - 15\%$  hotter than CR-2082 throughout the streamer belt region. As for the electron density products, CR-2208 was found to be  $\approx 15 - 20\%$  less dense than CR-2082 throughout the streamer belt region. These systematic differences are beyond the uncertainty level in the DENT products due to systematic sources (radiometric calibration and tomographic regularization), that Lloveras *et al.* (2017) estimated to be  $\lesssim 5\%$  and  $\approx 2\%$  for the electron temperature and density, respectively.

I would like to say something about Figure 10. Maybe the weird tale in AWSoM Ne in the poles. Ideas?

## References

- Aschwanden, M.J.: 2004, *Physics of the Solar Corona. An Introduction*, Praxis Publishing Ltd, ??? ADS.
- Aschwanden, M.J., Schrijver, C.J.: 2002, Analytical Approximations to Hydrostatic Solutions and Scaling Laws of Coronal Loops. *Astrophys. J. Suppl.* **142**(2), 269. DOI. ADS.
- Del Zanna, G., Dere, K.P., Young, P.R., Landi, E., Mason, H.E.: 2015, CHIANTI - An atomic database for emission lines. Version 8. *Astron. Astrophys.* **582**, A56. DOI. ADS.
- Frazin, R.A.: 2000, Tomography of the Solar Corona. I. A Robust, Regularized, Positive Estimation Method. *Astrophys. J.* **530**, 1026. DOI. ADS.
- Frazin, R.A., Vázquez, A.M., Kamalabadi, F.: 2009, Quantitative, Three-dimensional Analysis of the Global Corona with Multi-spacecraft Differential Emission Measure Tomography. *Astrophys. J.* **701**, 547. DOI. ADS.
- Huang, Z., Frazin, R.A., Landi, E., Manchester, W.B., Vázquez, A.M., Gombosi, T.I.: 2012, Newly Discovered Global Temperature Structures in the Quiet Sun at Solar Minimum. *Astrophys. J.* **755**, 86. DOI. ADS.
- Landi, E., Young, P.R., Dere, K.P., Del Zanna, G., Mason, H.E.: 2013, CHIANTI - An Atomic Database for Emission Lines. XIII. Soft X-Ray Improvements and Other Changes. *Astrophys. J.* **763**, 86. DOI. ADS.
- Lloveras, D.G., Vázquez, A.M., Nuevo, F.A., Frazin, R.A.: 2017, Comparative Study of the Three-Dimensional Thermodynamical Structure of the Inner Corona of Solar Minimum Carrington Rotations 1915 and 2081. *Solar Phys.* **292**(10), 153. DOI. <https://doi.org/10.1007/s11207-017-1179-z>.
- Mac Cormack, C., Vázquez, A.M., López Fuentes, M., Nuevo, F.A., Landi, E., Frazin, R.A.: 2017, Energy Input Flux in the Global Quiet-Sun Corona. *Astrophys. J.* **843**, 70. DOI. ADS.
- Nuevo, F.A., Huang, Z., Frazin, R., Manchester, i. Ward B., Jin, M., Vázquez, A.M.: 2013, Evolution of the Global Temperature Structure of the Solar Corona during the Minimum between Solar Cycles 23 and 24. *Astrophys. J.* **773**(1), 9. DOI. ADS.
- Nuevo, F.A., Vázquez, A.M., Landi, E., Frazin, R.: 2015, Multimodal Differential Emission Measure in the Solar Corona. *Astrophys. J.* **811**(2), 128. DOI. ADS.
- Press, W.H., Teukolsky, S.A., Vetterling, W.T., Flannery, B.P.: 2002, *Numerical recipes in C++ : the art of scientific computing*. ADS.
- Schiff, A.J., Cranmer, S.R.: 2016, Explaining Inverted-temperature Loops in the Quiet Solar Corona with Magnetohydrodynamic Wave-mode Conversion. *Astrophys. J.* **831**(1), 10. DOI. ADS.
- Serio, S., Peres, G., Vaiana, G.S., Golub, L., Rosner, R.: 1981, Closed coronal structures. II - Generalized hydrostatic model. *Astrophys. J.* **243**, 288. DOI. ADS.

- Spitzer, L.: 1962, *Physics of Fully Ionized Gases*. ADS.
- Vázquez, A.M.: 2016, Seeing the solar corona in three dimensions. *Advances in Space Research* **57**, 1286. DOI.
- Vázquez, A.M., Frazin, R.A., Kamalabadi, F.: 2009, 3D Temperatures and Densities of the Solar Corona via Multi-Spacecraft EUV Tomography: Analysis of Prominence Cavities. *Solar Phys.* **256**(1-2), 73. DOI. ADS.
- Vázquez, A.M., Frazin, R.A., Manchester, I. Ward B.: 2010, The Solar Minimum Corona from Differential Emission Measure Tomography. *Astrophys. J.* **715**(2), 1352. DOI. ADS.